




## Article

# A High Refractive Index Plasmonic Micro-Channel Sensor Based on Photonic Crystal Fiber

Jiangtao Lv <sup>1,2</sup>, Tong Liang <sup>1,2</sup>, Qiongchan Gu <sup>1</sup>, Qiang Liu <sup>1</sup>, Yu Ying <sup>3</sup>  and Guangyuan Si <sup>4,\*</sup><sup>1</sup> College of Information Science and Engineering, Northeastern University, Shenyang 110004, China<sup>2</sup> Hebei Key Laboratory of Micro-Nano Precision Optical Sensing and Measurement Technology, Qinhuangdao 066004, China<sup>3</sup> College of Information and Control Engineering, Shenyang Jianzhu University, Shenyang 110168, China<sup>4</sup> Melbourne Centre for Nanofabrication, Victorian Node of the Australian National Fabrication Facility, Clayton, VIC 3168, Australia

\* Correspondence: guangyuansi.si@nanomelbourne.com

**Abstract:** A new concave shaped high refractive index plasmonic sensor with a micro-channel is proposed in this work, which comprises an analyte channel in the core hole. The sensor is elaborately designed to reduce the interference effect from the metal coating. Furthermore, the impact of the proposed structure on the sensitivity is also investigated by engineering the geometric parameters. Gold is widely used to fabricate plasmonic and metamaterial devices because of its chemical stability and compatibility. According to wavelength interrogation technique, this sensor can obtain a maximal wavelength sensitivity of 10,050 nm/RIU. In view of the excellent indicators of this sensor, it has important development potential in chemical and biological research fields.

**Keywords:** micro-channel; high analyte refractive index; confinement loss



**Citation:** Lv, J.; Liang, T.; Gu, Q.; Liu, Q.; Ying, Y.; Si, G. A High Refractive Index Plasmonic Micro-Channel Sensor Based on Photonic Crystal Fiber. *Nanomaterials* **2022**, *12*, 3764. <https://doi.org/10.3390/nano12213764>

Academic Editor: Richard Jackman

Received: 5 October 2022

Accepted: 24 October 2022

Published: 26 October 2022

**Publisher's Note:** MDPI stays neutral with regard to jurisdictional claims in published maps and institutional affiliations.



**Copyright:** © 2022 by the authors. Licensee MDPI, Basel, Switzerland. This article is an open access article distributed under the terms and conditions of the Creative Commons Attribution (CC BY) license (<https://creativecommons.org/licenses/by/4.0/>).

## 1. Introduction

Surface plasmon resonance (SPR) can help detect environmental changes through evanescent waves [1]. SPR sensors play the most important role in sensing and monitoring food safety, drug development, environmental pollution, life science and public safety, etc. [2–4]. Kretschmann structure is commonly used in previous SPR sensor designs, which is characterized by depositing a metal layer on a prism substrate. However, the prism based SPR sensor cannot be further applied due to its structural limitations. Various fiber-based SPR sensors have advantages over prisms. However, among many optical fiber sensors, photonic crystal fiber (PCF) sensors are preferred by researchers due to their high integration, design flexibility, and great miniaturization potential [5–7].

In previous academic reports, precious metals such as gold (Au) and silver (Ag) with excellent plasmonic characteristics are used for various SPR sensors. Although Ag provides high detection accuracy and sensitivity, Au exhibits better stability advantages. An internally metal-coated sensor is difficult to manufacture because it requires the metal and analyte to be inserted into micron-sized air holes [8]. In contrast, the externally metal-coated PCF sensor is not only easy to manufacture but also able to offer more design possibilities. Researchers have found that the D-type fiber has a higher sensitivity and excellent structural performance [9–13]. However, the D-type fiber is also difficult to manufacture. In addition to manufacturing difficulties, high refractive index (RI) detection is another obstacle in PCF sensors. As we all know, the detection range is usually less than 1.42 for most common PCF sensors [14–16]. In order to achieve high RI sensing, a hollow PCF fiber core can be filled with analyte to form a waveguide [17]. Therefore, there is great potential in designing high RI sensors using this method.

## 2. Materials and Methods

Here, we design a novel micro-channel assisted D-type hollow PCF-SPR sensor. The hollow core structure of the designed sensor can achieve high RI detection for liquid analytes, and the addition of micro-channels in a D-type PCF can significantly reduce the difficulty of polishing. Moreover, the non-direct contact between the plasmonic materials and the analyte can further minimize the interference effects. As a result, the sensor shows the advantages of favorable sensitivity and real-time sensing in the performance measuring methods.

The scheme of the concave shaped high RI plasmonic sensor is illustrated in Figure 1. The diameter of the analyte-core is much larger than the diameter of the surrounding pores. The micro-channel is designed on the polished surface and directly located above the core. Furthermore, the micro-channel is coated with Au, acting as the plasmonic material. With the help of COMSOL Multiphysics software, the sensing performance of the proposed device is simulated by finite element method. The whole model is constructed by using the super thinning standard of free triangle mesh. The complete mesh consists of 22,228 domain elements and 1246 boundary elements. The critical parameters are pore diameter ( $d$ ), analyte-core diameter ( $d_c$ ), pore spacing ( $\Lambda$ ), Au layer thickness ( $t_g$ ), and micro-channel radius ( $r$ ). Au is evenly coated on the channel surface, which cannot only avoid direct contact with the analyte but also facilitate real-time sensing. Moreover, absorbing light reflection can improve the accuracy of results through perfectly matched layer (PML). The RI of fused silica is calculated as follows [18–21]:

$$n^2(\lambda) = 1 + \frac{B_1\lambda^2}{\lambda^2 - C_1} + \frac{B_2\lambda^2}{\lambda^2 - C_2} + \frac{B_3\lambda^2}{\lambda^2 - C_3} \quad (1)$$

where  $B_1 = 0.696166300$ ,  $B_2 = 0.407942600$ ,  $B_3 = 0.897479400$ ,  $C_1 = 4.6791482626 \times 10^{-3} \mu\text{m}^2$ ,  $C_2 = 1.35120631 \times 10^{-2} \mu\text{m}^2$ , and  $C_3 = 97.9340025 \mu\text{m}^2$ .

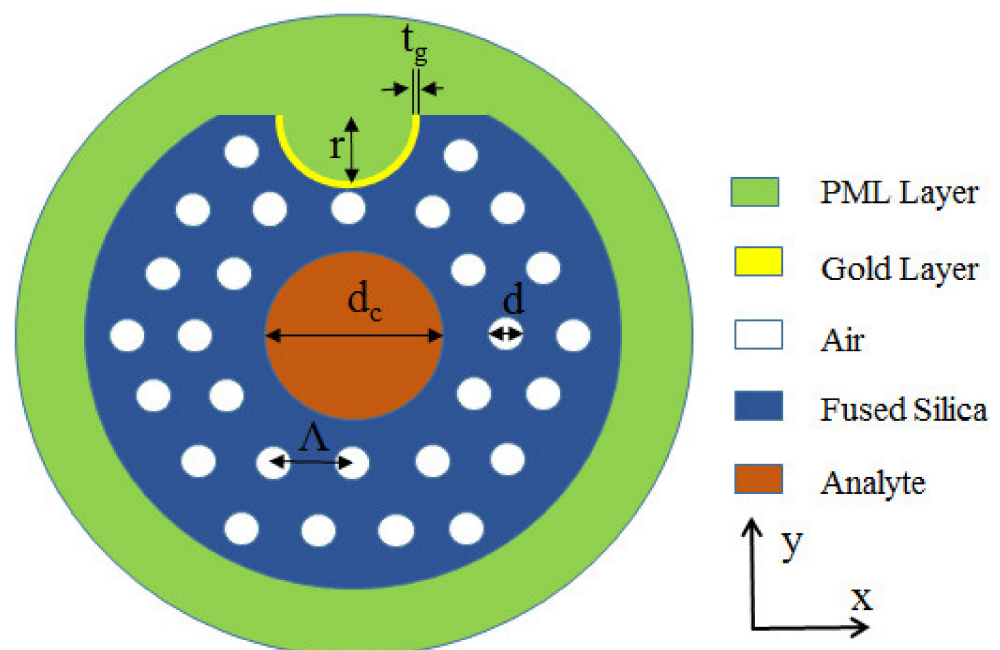


**Figure 1.** Geometry with labeled pore diameter ( $d$ ), analyte-core diameter ( $d_c$ ), pore spacing ( $\Lambda$ ), Au layer thickness ( $t_g$ ), and micro-channel radius ( $r$ ).

The confinement loss is evaluated as follows [22–24]:

$$\alpha(x, y) = 8.686 \times \frac{2\pi}{\lambda} \times \text{Im}(n_{\text{eff}}) \times 10^4 \quad (2)$$

where  $\lambda$  is the wavelength in  $\mu\text{m}$ , and  $\text{Im}(n_{\text{eff}})$  is the imaginary part of the effective RI.

### 3. Results and Discussion

The electric field distribution of the fundamental core mode, surface plasmon polariton (SPP) mode, and the resonance coupling mode of the proposed sensor is plotted in Figure 2. The structural parameters of electric field distribution simulation conditions are  $d_c = 5 \mu\text{m}$ ,  $d = 0.7 \mu\text{m}$ ,  $\Lambda = 2.1 \mu\text{m}$ ,  $r = 2 \mu\text{m}$ , and  $t_g = 30 \text{ nm}$ . It can be seen clearly from Figure 2 that three fundamental modes are revealed in (a), (b), and (c), respectively. Different fundamental modes lead to different energy distributions. Figure 3 illustrates the changes of loss spectra and RI of the two modes (core and SPP) when the analyte RI is 1.45. The curves of the two modes fall in a nearly straight line and intersect at  $1.15 \mu\text{m}$  midway. At this resonance condition, the coupling between the two modes is the strongest, which leads to a sharp resonance peak.

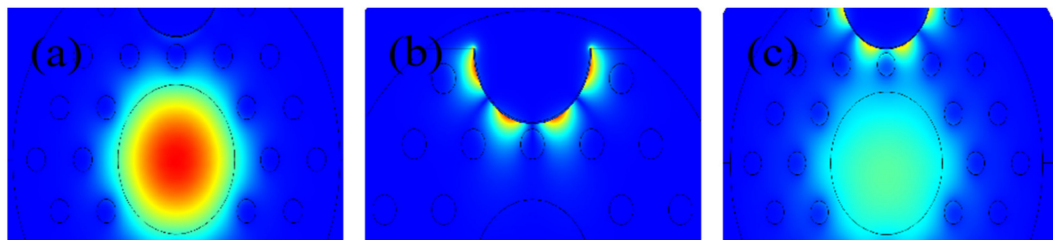


**Figure 2.** Electric field distribution showing optical coupling strength of (a) core mode, (b) SPP mode, and (c) the resonance coupling mode.

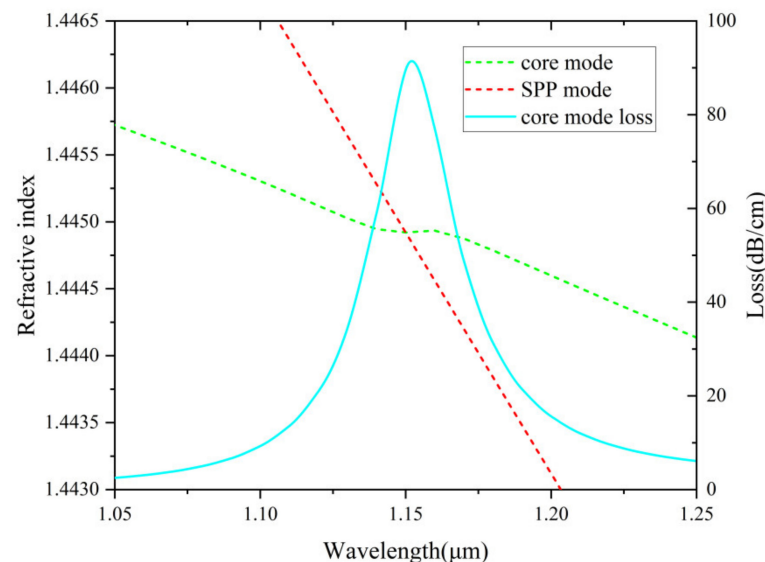


**Figure 3.** The change of loss spectrum and refractive index of the two modes (core and SPP) at  $n_a = 1.45$  as a function of wavelength.

In Figure 4, the effect of loss spectra is also examined when the RI of analyte is varied from 1.43 to 1.49. As can be seen, when the  $n_a$  value is very high, the illustration shows that the peak loss value is extremely low. The loss depth represents the coupling degree of the core and SPP modes. Different  $n_a$  values lead to different resonance conditions so that the peak wavelength blue shifts. When  $n_a$  becomes higher, the loss spectra decrease rapidly. Figure 4 shows that the detection range of this sensor is higher than 1.42, which is

excellent for most commonly used PCF sensors. This is because the analyte is placed in the fiber core to form a waveguide so that the analyte with a higher RI than the background material can be detected.

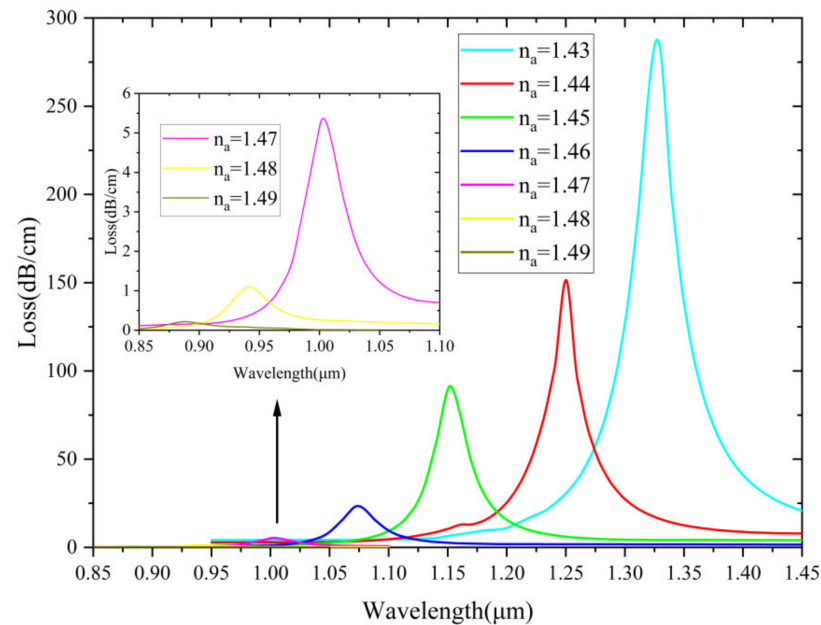


**Figure 4.** The loss spectrum of the core mode with different  $n_a$  from 1.43 to 1.49.

The wavelength sensitivity is evaluated as follows [25]:

$$S_{\lambda} (\text{nm/RIU}) = \Delta\lambda_{\text{peak}} / \Delta n_a \quad (3)$$

where  $\Delta\lambda_{\text{peak}}$  indicates the resonance wavelength shifts and  $\Delta n_a$  represents the change of analyte RI.

Along with wavelength sensitivity, sensor resolution is considered as another important performance parameter. The sensor resolution is calculated as follows [26]:

$$R(\text{RIU}) = \Delta n_a \Delta\lambda_{\text{min}} / \Delta\lambda_{\text{peak}} \quad (4)$$

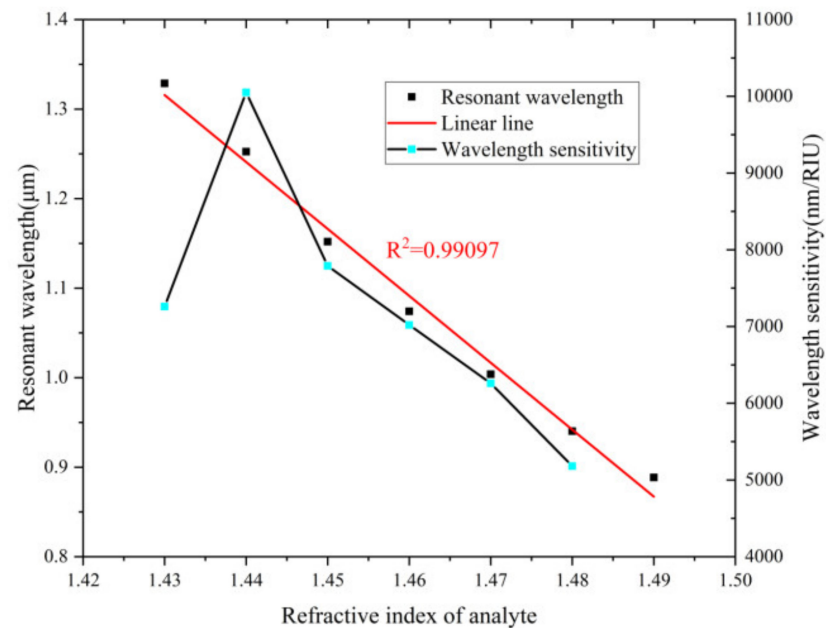
where  $\Delta\lambda_{\text{min}} = 0.1 \text{ nm}$  (minimum spectral resolution). The maximum resolution of the proposed sensor is obtained as  $9.95 \times 10^{-6} \text{ RIU}$ . Therefore, it shows that the measurement scale of the minute change in the RI of the analyte detected by the sensor is  $10^{-6}$ .

The figure of merit (FOM) is calculated as follows [27]:

$$\text{FOM} = S_{\lambda} / \text{FWHM} \quad (5)$$

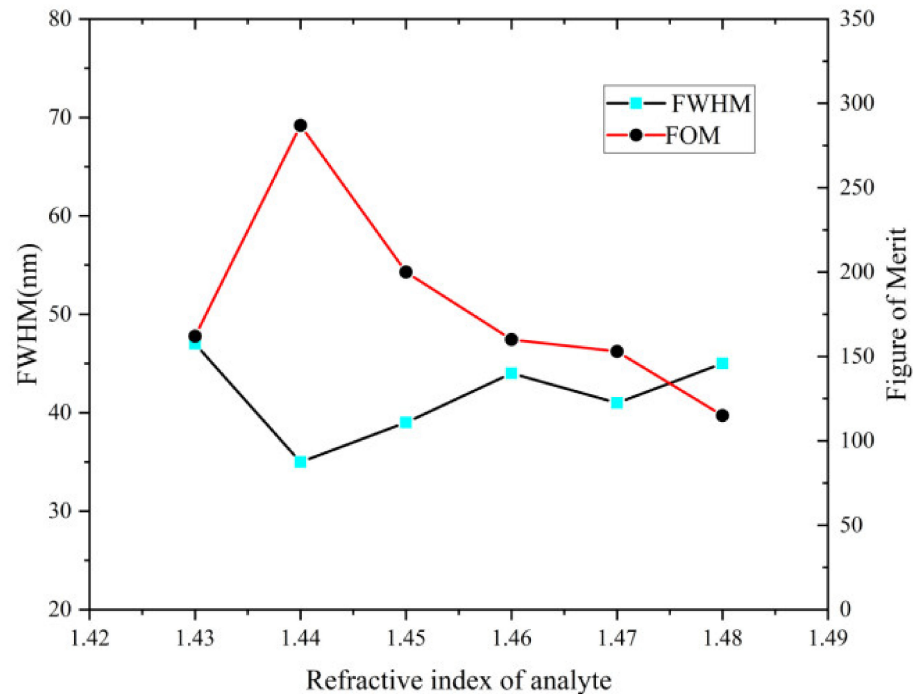
where FWHM is the full width at half maximum of the loss spectrum.

Figure 5 depicts the change trend of resonance wavelength and wavelength sensitivity. The sensor shows a good linearity ( $R^2$  is 0.99097) with analyte RI from 1.43 to 1.49. High linearity is regarded as a sign of a functional sensor. The highest sensitivity that can be obtained is 10,050 nm/RIU ( $n_a = 1.44$ ).



**Figure 5.** The resonance wavelength and wavelength sensitivity as a function of  $n_a$ .

Figure 6 depicts the change trend of FOM and FWHM values with varying  $n_a$ . The overall FOM shows a downward trend except for a brief rise from 1.43 to 1.44. The FWHM reveals the opposite trend, which is that these two parameters are reciprocal to each other. The sensor displays the highest value of FOM ( $287 \text{ RIU}^{-1}$ ) with  $n_a = 1.44$ .



**Figure 6.** FWHM and FOM variation as a function of  $n_a$ .

In order to find out the optimal structural parameters, analyte RI with 1.45 and 1.46 is further considered. Variation of the analyte-core diameter  $d_c$  is shown in Figure 7, for  $d_c$  values from  $2.4 \mu\text{m}$  to  $2.6 \mu\text{m}$ . Before optimizing  $d_c$ , the other structural parameters remain unchanged. Increasing  $d_c$  can improve the resolution and obtain lower FWHM. According to the observation of the curves in the figure, the size of the analyte-core diameter has little

interference with the sensor. Therefore, by taking into account the confinement loss value and low FWHM,  $d_c = 5 \mu\text{m}$  is considered as the optimized parameter.

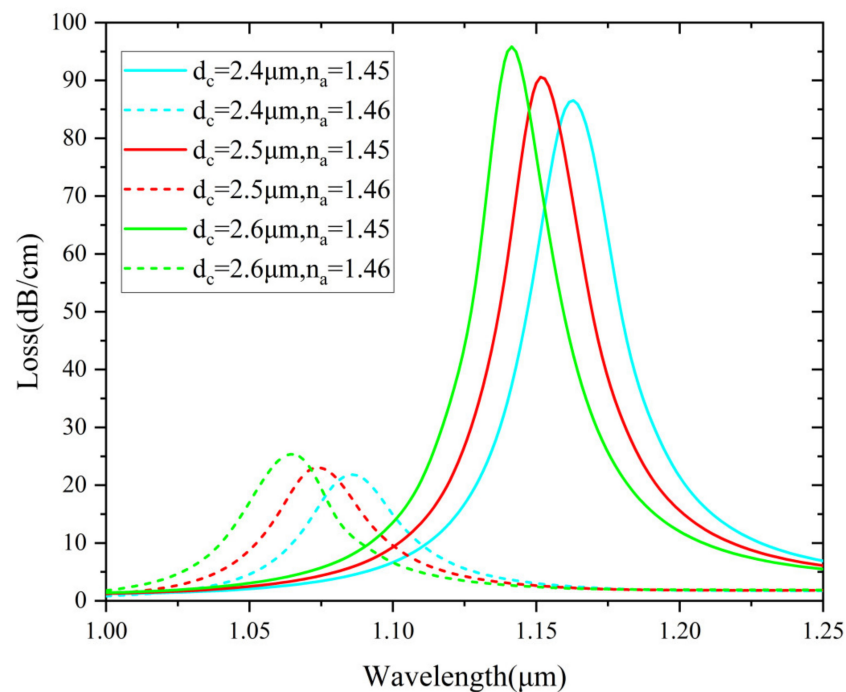


**Figure 7.** Loss spectra ( $n_a = 1.45$  and  $1.46$ ) for different  $d_c$  of  $2.4$ ,  $2.5$ , and  $2.6 \mu\text{m}$ .

In the numerical simulations, the pore diameter  $d$  is also closely related to the confinement loss and resonant wavelength. Figure 8 illustrates the loss spectra of different  $d$  of  $0.7$ ,  $0.8$ , and  $0.9 \mu\text{m}$ . The resonant wavelength begins to shift rapidly as the pore diameter increases. It can be concluded that the loss spectra of different pore diameters vary obviously under different RI. Therefore,  $d = 0.7 \mu\text{m}$  is considered as the optimized value by taking into account both the sensitivity and FWHM.

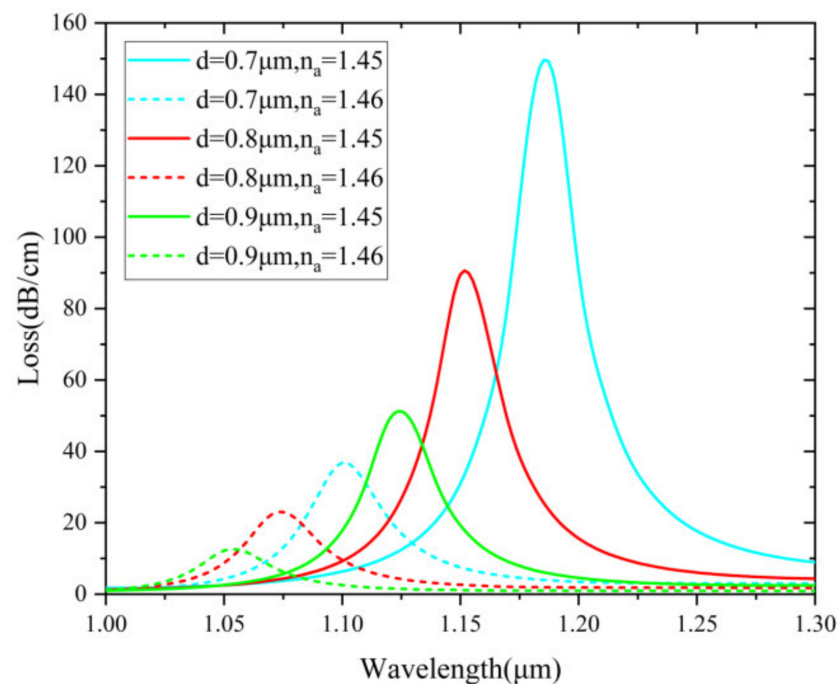


**Figure 8.** Loss spectra ( $n_a = 1.45$  and  $1.46$ ) for different  $d$  of  $0.7$ ,  $0.8$ , and  $0.9 \mu\text{m}$ .



In Figure 9, the effect of varying pore spacing is investigated. The resonant wavelength shifts dramatically first and then slowly as the pore spacing increases, which is because the phase-matching condition is changed. Moreover, with increasing pitch, the confinement loss increases accordingly. This is because the coupling strength with the plasmonic material is more intense after the spacing increases. Considering the strength of the coupling and sensing performances,  $\Lambda = 2.1 \mu\text{m}$  is determined as the optimized parameter.

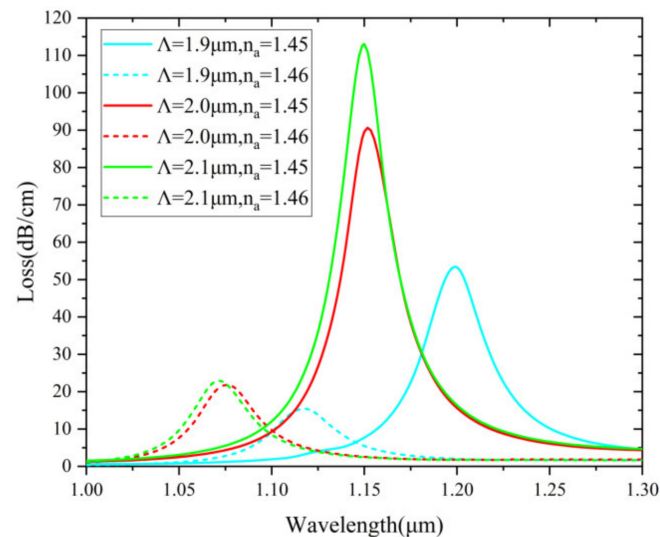


**Figure 9.** Loss spectra ( $n_a = 1.45$  and  $1.46$ ) when  $\Lambda$  is varied from  $1.9$  to  $2.1 \mu\text{m}$ .

In Figure 10, the effect of varying micro-channel radius ( $r$ ) is examined from  $1.9 \mu\text{m}$  to  $2.1 \mu\text{m}$ . When  $r$  increases, SPR effect boosts. This results in the increase of the loss value. The wavelength sensitivities are  $8000$ ,  $8400$ , and  $8150 \text{ nm/RIU}$ , respectively. The optimized value is considered as  $2 \mu\text{m}$  by taking into account the sensing response stability. The proposed sensor is easier to design the thickness and location of the Au layer than most internally coated PCF sensors. This advantage makes the proposed sensor stand out and further enables fabrication possibilities. Figure 11 shows loss spectra ( $n_a = 1.45$  and  $1.46$ ) when  $t_g$  is varied from  $30$  to  $50 \text{ nm}$  ( $10 \text{ nm}$  intervals). It is clearly observed that the resonant wavelength red shifts and loss depth reduces notably with increasing  $t_g$  for  $n_a = 1.45$ . The calculated wavelength sensitivities are  $8150$ ,  $8000$ , and  $7900 \text{ nm/RIU}$ , respectively. Considering the sensitivity and FWHM,  $t_g = 30 \text{ nm}$  is determined as the optimized value.

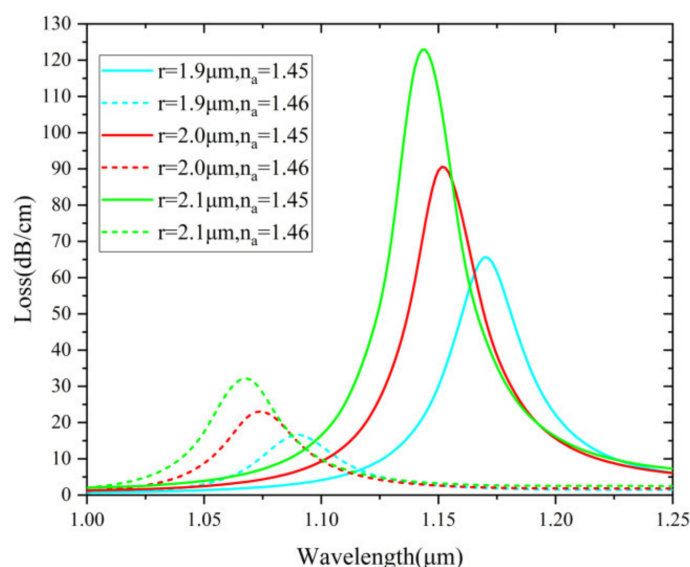


**Figure 10.** Loss spectra ( $n_a = 1.45$  and  $1.46$ ) when  $r$  is varied from  $1.9$  to  $2.1 \mu\text{m}$ .

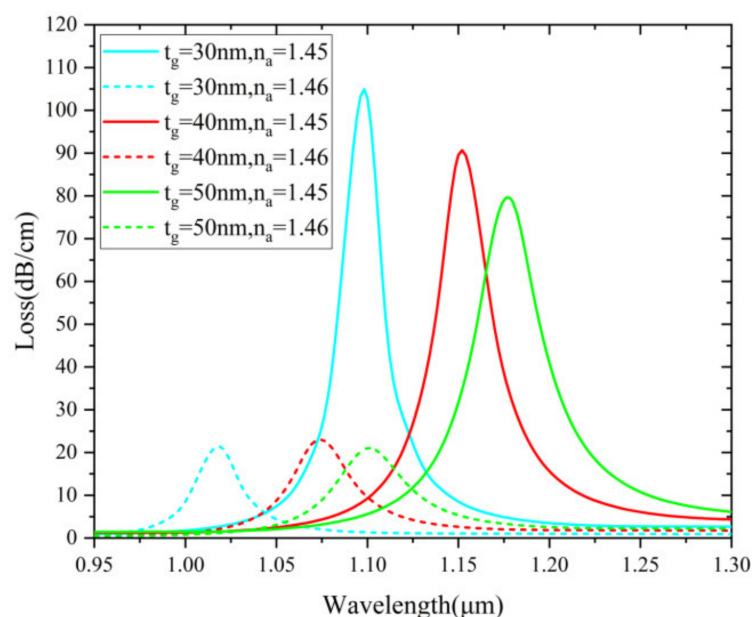


Figure 11. Loss spectra ( $n_a = 1.45$  and  $1.46$ ) when  $t_g$  is varied from 30 to 50 nm.

#### 4. Conclusions

In conclusion, we have designed a concave shaped high RI plasmon-assisted sensor with a micro-channel design. The proposed device has the special advantage of detecting high analyte RI and avoiding direct contact between analyte and the metal layer. The calculated results show that geometrical parameters possess a significant impact on device performances. Under the optimized structural conditions, the proposed sensor demonstrates the highest sensitivity of  $10,050 \text{ nm/RIU}$  with a  $9.95 \times 10^{-6} \text{ RIU}$  sensing resolution. The FOM of  $287 \text{ RIU}^{-1}$  and the high linearity of  $0.99097$  are realized with  $n_a$  from  $1.43$  to  $1.49$ . The results show that the sensor has useful potential for high refractive index detection of chemical and biological liquids.

**Author Contributions:** Conceptualization, T.L. and J.L.; methodology, T.L.; formal analysis, T.L. and G.S.; writing, T.L. and J.L.; review and editing, Q.G. and G.S.; supervision, Y.Y. and Q.L. All authors have read and agreed to the published version of the manuscript.

**Funding:** This research was funded by National Natural Science Foundation of China (Grant No. 62105058), the Natural Science Foundation of Hebei Province (Grant No. F2018501063), Hebei Province Science and Technology Plan Key Research and Development Project Research Funds (Grant No. 18273902D) and the Fundamental Research Funds for the Central Universities Key Scientific Research Guidance Project (Grant No. N2023005). This work was performed in part at the Melbourne Center for Nanofabrication (MCN) in the Victorian Node of the Australian National Fabrication Facility (ANFF).

**Institutional Review Board Statement:** Not applicable.

**Informed Consent Statement:** Not applicable.

**Data Availability Statement:** Not applicable.

**Conflicts of Interest:** The authors declare no conflict of interest.

#### References

1. An, G.; Li, S.; Zhang, W.; Fan, Z.; Bao, Y. A polarization filter of gold-filled photonic crystal fiber with regular triangular and rectangular lattices. *Opt. Commun.* **2014**, *331*, 316–319. [\[CrossRef\]](#)
2. Wang, Q.; Zhao, W.M. Optical methods of antibiotic residues detections: A comprehensive review. *Sens. Actuators B Chem.* **2018**, *269*, 238–256. [\[CrossRef\]](#)
3. Singh, S.; Prajapati, Y. Highly sensitive dual-core symmetrical side-polished modified D-shaped SPR based PCF refractive index sensor with deeply etched micro openings. *Optik* **2021**, *235*, 166657. [\[CrossRef\]](#)



4. Wang, Q.; Jing, J.; Wang, B. Highly Sensitive SPR Biosensor Based on Graphene Oxide and Staphylococcal Protein A Co-Modified TFBG for Human IgG Detection. *IEEE Trans. Instrum. Meas.* **2019**, *68*, 3350–3357. [[CrossRef](#)]
5. Wang, G.; Lu, Y.; Duan, L.; Yao, J. A Refractive Index Sensor Based on PCF With Ultra-Wide Detection Range. *IEEE J. Sel. Top. Quantum Electron.* **2020**, *27*, 5600108. [[CrossRef](#)]
6. Haque, E.; Hossain, M.A.; Ahmed, F.; Namihiro, Y. Surface Plasmon Resonance Sensor Based on Modified D-Shaped Photonic Crystal Fiber for Wider Range of Refractive Index Detection. *IEEE Sens. J.* **2018**, *18*, 8287–8293. [[CrossRef](#)]
7. Cheng, T.; Li, X.; Li, S.; Yan, X.; Zhang, X.; Wang, F. Surface plasmon resonance temperature sensor based on a photonic crystal fiber filled with silver nanowires. *App. Opt.* **2020**, *59*, 5108–5113. [[CrossRef](#)] [[PubMed](#)]
8. Yu, X.; Zhang, Y.; Pan, S.; Shum, P.; Yan, M.; Leviatan, Y.; Li, C. A selectively coated photonic crystal fiber based surface plasmon resonance sensor. *J. Opt.* **2010**, *12*, 015005. [[CrossRef](#)]
9. Paul, A.K.; Sarkar, A.K.; Islam, M.H.; Morshed, M. Dual core photonic crystal fiber based surface plasmon resonance biosensor. *Optik* **2018**, *170*, 400–408. [[CrossRef](#)]
10. Liang, H.; Shen, T.; Feng, Y.; Liu, H.C.; Han, W. A D-Shaped Photonic Crystal Fiber Refractive Index Sensor Coated with Graphene and Zinc Oxide. *Sensors* **2021**, *21*, 71. [[CrossRef](#)] [[PubMed](#)]
11. Zha, F.; Li, J.; Sun, P.; Ma, H. Highly sensitive selectively coated D-shape photonic crystal fibers for surface plasmon resonance sensing. *Phys. Lett. A* **2019**, *383*, 1825–1830. [[CrossRef](#)]
12. Dash, J.N.; Jha, R. On the performance of graphene-based D-shaped photonic crystal fiber biosensor using surface plasmon resonance. *Plasmonics* **2015**, *10*, 1123–1131. [[CrossRef](#)]
13. Liu, Q.; Yan, B.; Liu, J. U-shaped photonic quasi-crystal fiber sensor with high sensitivity based on surface plasmon resonance. *Appl. Phys. Express* **2019**, *12*, 052014. [[CrossRef](#)]
14. Tian, M.; Lu, P.; Chen, L.; Lv, C.; Liu, D. All-solid dshaped photonic fiber sensor based on surface plasmon resonance. *Opt. Commun.* **2012**, *285*, 1550–1554. [[CrossRef](#)]
15. Hossen, M.N.; Ferdous, M.; Khalek, M.A.; Chakma, S.; Paul, B.K.; Ahmed, K. Design and analysis of biosensor based on surface plasmon resonance. *Sens. Bio-Sens. Res.* **2018**, *21*, 1–6. [[CrossRef](#)]
16. An, G.; Hao, X.; Li, S.; Yan, X.; Zhang, X. D-shaped photonic crystal fiber refractive index sensor based on surface plasmon resonance. *Appl. Opt.* **2017**, *56*, 6988–6992. [[CrossRef](#)] [[PubMed](#)]
17. Liu, B.; Jiang, Y.; Zhu, X.; Tang, X.; Shi, Y. Hollow fiber surface plasmon resonance sensor for the detection of liquid with high refractive index. *Opt. Exp.* **2013**, *21*, 32349–32357.
18. Luan, N.; Zhao, L.; Lian, Y.; Lou, S. A high refractive index plasmonic sensor based on D-shaped photonic crystal fiber with laterally accessible hollow-core. *IEEE Photonics J.* **2018**, *10*, 1–7. [[CrossRef](#)]
19. Paul, A.K.; Sarkar, A.K.; Khaleque, A. Dual-Core Photonic Crystal Fiber Plasmonic Refractive Index Sensor: A Numerical Analysis. *Photonic Sens.* **2019**, *9*, 151–161. [[CrossRef](#)]
20. Ghahramani, S.; Barvestani, J.; Meshginqalam, B. High-performance opening-up dual-core photonic crystal fiber sensors based on surface plasmon resonance. *Plasmonics* **2021**, *17*, 181–191. [[CrossRef](#)]
21. Akowuah, E.K.; Gorman, T.; Ademgil, H.; Haxha, S.; Robinson, G.K.; Oliver, J. Numerical Analysis of a Photonic Crystal Fiber for Biosensing Applications. *IEEE J. Quantum Electron.* **2012**, *48*, 1403–1410. [[CrossRef](#)]
22. Guo, X.; Han, L.; Liu, F.; Li, S. Refractive index sensing characteristics of dual-core PCF based on surface plasmon resonance. *Opt. Int. J. Light Electron. Opt.* **2020**, *218*, 164796. [[CrossRef](#)]
23. Wu, J.; Li, S.; Shi, M.; Feng, X. Photonic crystal fiber temperature sensor with high sensitivity based on surface plasmon resonance. *Opt. Fiber Technol.* **2018**, *43*, 90–94. [[CrossRef](#)]
24. Rifat, A.A.; Ahmed, R.; Mahdiraji, G.A.; Adikan, F.R.M. Highly Sensitive D-Shaped Photonic Crystal Fiber-Based Plasmonic Biosensor in Visible to Near-IR. *IEEE Sens. J.* **2017**, *17*, 2776–2783. [[CrossRef](#)]
25. Danlard, I.; Akowuah, E.K. Assaying with PCF-based SPR refractive index biosensors: From recent configurations to outstanding detection limits. *Opt. Fiber Technol.* **2020**, *54*, 102083. [[CrossRef](#)]
26. Hasan, M.R. Spiral Photonic Crystal Fiber-Based Dual-Polarized Surface Plasmon Resonance Biosensor. *IEEE Sens. J.* **2018**, *18*, 133–140. [[CrossRef](#)]
27. Lou, J.; Cheng, T.; Li, S.; Zhang, X. Surface plasmon resonance photonic crystal fiber biosensor based on gold-graphene layers. *Opt. Fiber Technol.* **2019**, *50*, 206–211. [[CrossRef](#)]